Integrating Automated Electrochemistry and High-Throughput Characterization with Machine Learning to Explore Si–Ge–Sn Thin-Film Lithium Battery Anodes

Alexey Sanin,* Jackson K. Flowers, Tobias H. Piotrowiak, Frederic Felsen, Leon Merker, Alfred Ludwig, Dominic Bresser, and Helge Sören Stein*

High-performance batteries need accelerated discovery and optimization of new anode materials. Herein, we explore the Si–Ge–Sn ternary alloy system as a candidate fast-charging anode materials system by utilizing a scanning droplet cell (SDC) as an autonomous electrochemical characterization tool with the goal of subsequent upscaling. As the SDC is performing experiments sequentially, an exploration of the entire ternary space is unfeasible due to time constraints. Thus, closed-loop optimization, guided by real-time data analysis and sequential learning algorithms, is utilized to direct experiments. The lead material identified is scaled up to a coin cell to validate the findings from the autonomous millimeter-scale thin-film electrochemical experimentation. Explainable machine learning (ML) models incorporating data from high-throughput Raman spectroscopy and X-ray diffraction (XRD) are used to elucidate the effect of short and long-range ordering on material performance.

1. Introduction

The electrification of transportation and the increasing demand for digital technologies necessitate a transformation in energy storage systems.[1,2] Novel chemistries and processing advancements in batteries are essential for electric vehicles and portable devices, as well as for buffering electrical grid demand and supply.[3] However, significant improvements in battery technology are required to meet the growing requirements for higher energy densities and faster charging times.[4]

High-performance, fast-charging anodes are at the forefront of advancements in battery technology, playing a critical role in achieving the high-power performance needed to meet the growing energy demands of modern applications.[4] Among potential anode materials for Li-storage, silicon (Si) stands out due to its exceptionally high theoretical capacity of up to 3578 mAh g^{-1} at room temperature,[5] almost ten times higher than for conventional graphite anodes. Pure Si still has major disadvantages, such as an extreme volume expansion of 390%[6] and overall slow

---

A. Sanin, J. K. Flowers, L. Merker, D. Bresser
Helmholtz Institute Ulm (HIU)
Helmholtzstr. 11, 89081 Ulm, Germany
E-mail: alexey.sanin@tum.de

A. Sanin, J. K. Flowers, L. Merker, D. Bresser
Karlsruhe Institute of Technology (KIT)
76021 Karlsruhe, Germany

A. Sanin, F. Felsen, L. Merker, H. S. Stein
Technical University of Munich (TUM)
TUM School of Natural Sciences
Department of Chemistry
Chair of Digital Catalysis
Lichtenbergstr. 4, 85748 Garching, Germany
E-mail: helge.stein@tum.de

© 2025 The Author(s). Advanced Energy Materials published by Wiley-VCH GmbH. This is an open access article under the terms of the Creative Commons Attribution License, which permits use, distribution and reproduction in any medium, provided the original work is properly cited.

A. Sanin, F. Felsen, L. Merker, H. S. Stein
Technical University of Munich (TUM)
Munich Data Science Institute (MDSI)
Walther-von-Dyck-Str. 10, 85748 Garching, Germany

A. Sanin, F. Felsen, L. Merker, H. S. Stein
Technical University of Munich (TUM)
Munich Institute of Robotics and Machine Intelligence (MIRMI)
Georg-Brauchle-Ring 60, 80992 Munich, Germany

A. Sanin, F. Felsen, L. Merker, H. S. Stein
Technical University of Munich (TUM)
Munich Institute of Integrated Materials
Energy and Process Engineering (MEP)
Lichtenbergstr. 4 a, 85748 Garching, Germany

A. Sanin, F. Felsen, L. Merker, H. S. Stein
Munich Center for Machine Learning (MCML)
Oettingenstraße 67, 80538 Munich, Germany

T. H. Piotrowiak, A. Ludwig
Ruhr University Bochum (RUB)
Institute for Materials
Chair for Materials Discovery and Interfaces
Universitätsstr. 150, 44780 Bochum, Germany

D. Bresser
Ulm University (UUlm)
89069 Ulm, Germany

kinetics. Besides tailoring the nano- and microstructure of the materials, tuning the chemical composition to improve kinetics is an alternative route to improve the electrochemical performance of Si-based anodes.[7,8] For this study, the Si—Ge—Sn alloy was chosen as a model system due to its group IV elements exhibiting similar properties and being known to alloy with Li.[9] While pure germanium (Ge) and tin (Sn) show lower specific capacities (up to 1624 and 993 mAh g^{-1}), mixing these elements may enhance the performance of anodes, as volume changes for Ge and Sn are smaller (up to ≈272 and 260%),[9] the diffusivity of Li in Ge and Sn at room temperature is a few orders of magnitudes higher than in Si (≈10^{-12} and 10^{-9}–10^{-7} vs 10^{-14} cm^2 s^{-1}, respectively).[10–12] Ge and Sn also provide higher electronic conductivity (≈10^0 and 10^5–10^7 vs 10^{-3} S m^{-1} for Si)[12,13] and, therefore, support operation at higher dis-/charge rates,[10] providing not only high energy but also higher power densities.

Discovering and developing new materials for batteries is time-intensive, and conventional battery cycling may take several weeks to months. Alternative inexpensive methods are needed to focus on electrochemical activity during the initial cycles when materials typically exhibit a performance close to theoretical values. They may also provide reliable proxies for long-term performance, serving as decision gates for further processing optimization. This approach enables faster evaluation of battery electrode electrochemical behavior within a shorter timeframe. The scanning droplet cell (SDC) is a miniaturized electrochemical cell designed for micro- and millimeter-scale electrochemical characterization, enabling rapid, automated, localized analysis.[14,15] It is particularly well-suited for materials library characterization with compositional gradients to systematically study the effects of chemical variation.[16–18] The three-electrode cell can separate contributions of the material of interest from those of the counter-electrode, simplifying comparative analysis. Full automation of the experimental process has been shown to reduce errors and increase reproducibility, leading to more reliable data.[16,19] Coupling autonomous experimentation with active learning (AL) algorithms for the decision-making of the next experiments could accelerate the discovery pace for exploration and optimization tasks.[20,21] Although an infrastructural framework for the SDC autonomous experimental orchestration using AL algorithms has been demonstrated,[21] it has not been adapted and demonstrated for new battery materials exploration. Moreover, the question remains whether the insights gained at the millimeter-scale through SDC testing can be successfully transferred to larger scales, ultimately advancing the technology readiness level (TRL) and paving the way for eventual commercialization.

In this context, building efficient workflows — sequences of interconnected and potentially accelerated research tasks or processes[22] — is essential for accelerating the discovery and optimization of energy storage materials over different TRLs. These workflows can be designed as a part of self-driving laboratories, which focus on autonomous, real-time feedback-driven experimentation, and materials acceleration platforms,[23–27] broader collaborative infrastructures that integrate diverse methodologies. They can combine autonomous experimentation, computational tools, data analysis tools, quality control, and proper data management to speed up materials discovery with minimal human interaction within a single laboratory and at interlabora-

tory levels. Using high-throughput (HT) experimentation in the experimental workflows enables the rapid exploration of multidimensional compositional and parameter spaces, facilitating the identification of high-performance materials and generating extensive datasets for ML-driven insights.[28] While HT methods are effective for broad exploration and unraveling trends and correlations, they are resource-intensive and less efficient for targeted optimization. In contrast, closed-loop data-driven autonomous experimentation succeeds in optimization tasks, as it iteratively uses feedback from experimental results to effectively refine specific material properties.[29] The trade-off between these two methods can be addressed by combining the strengths of both approaches in a single experimental workflow for different tasks: using more exploitative closed-loop experimentation for optimizing the target parameter while applying more explorative HT methods to understand the physicochemical relationships.

Herein, we present the implementation of the comprehensive experimental workflow for synthesis and data-driven closed-loop autonomous electrochemical characterization to find high-capacity Si-based materials suitable for high-energy and fast-charging applications (**Figure 1**). The findings were upscaled for approach verification. A systematic high-throughput investigation of the chemical, vibrational, and structural properties was performed to find correlations and causations between different properties and explain the differences in materials performance using ML algorithms. This combined approach aims to significantly accelerate the development of next-generation anode materials suitable for high-performance, fast-charging batteries.

2. Results and Discussion

2.1. Materials Library Synthesis

To demonstrate and validate the experimental approach, achieving a broad compositional distribution within the materials library is essential for effective system exploration. Given that Sn has a higher deposition rate,[30] low-power radio-frequency (RF) sputtering was used for Sn, while high-power direct current (DC) sputtering was applied for Si. A high working gas pressure was chosen for the deposition to enhance compositional variation across the materials library. This approach reduces the mean free path of sputtered atoms due to collisions with Ar atoms, leading to higher deposition yields near the sputter target and lower rates in distant regions. As a result, the synthesized materials libraries span compositional ranges of ≈50% for all elements (Si$_x$Ge$_y$Sn$_z$, x = 0.15–0.63, y = 0.15–0.68, z = 0.10–0.64) and thicknesses between 90–150 nm (Figure S3c, Supporting Information). To ensure that observed variations in electrochemical behavior were primarily due to compositional differences rather than film thickness, we maintained a uniform thickness range across the materials library. Thinner films in the 100-nm range help reduce diffusion limitations and mechanical stresses that can arise in thicker films,[31,32] allowing for a more accurate assessment of the intrinsic material properties. This approach minimizes variations in thickness as a variable in the design space to simplify the analysis of near-intrinsic composition–structure–property relationships. Additionally, the thin-film configuration could promote the investigation of the intrinsic behavior of the active material, eliminating the effects of binders and conductive additives.
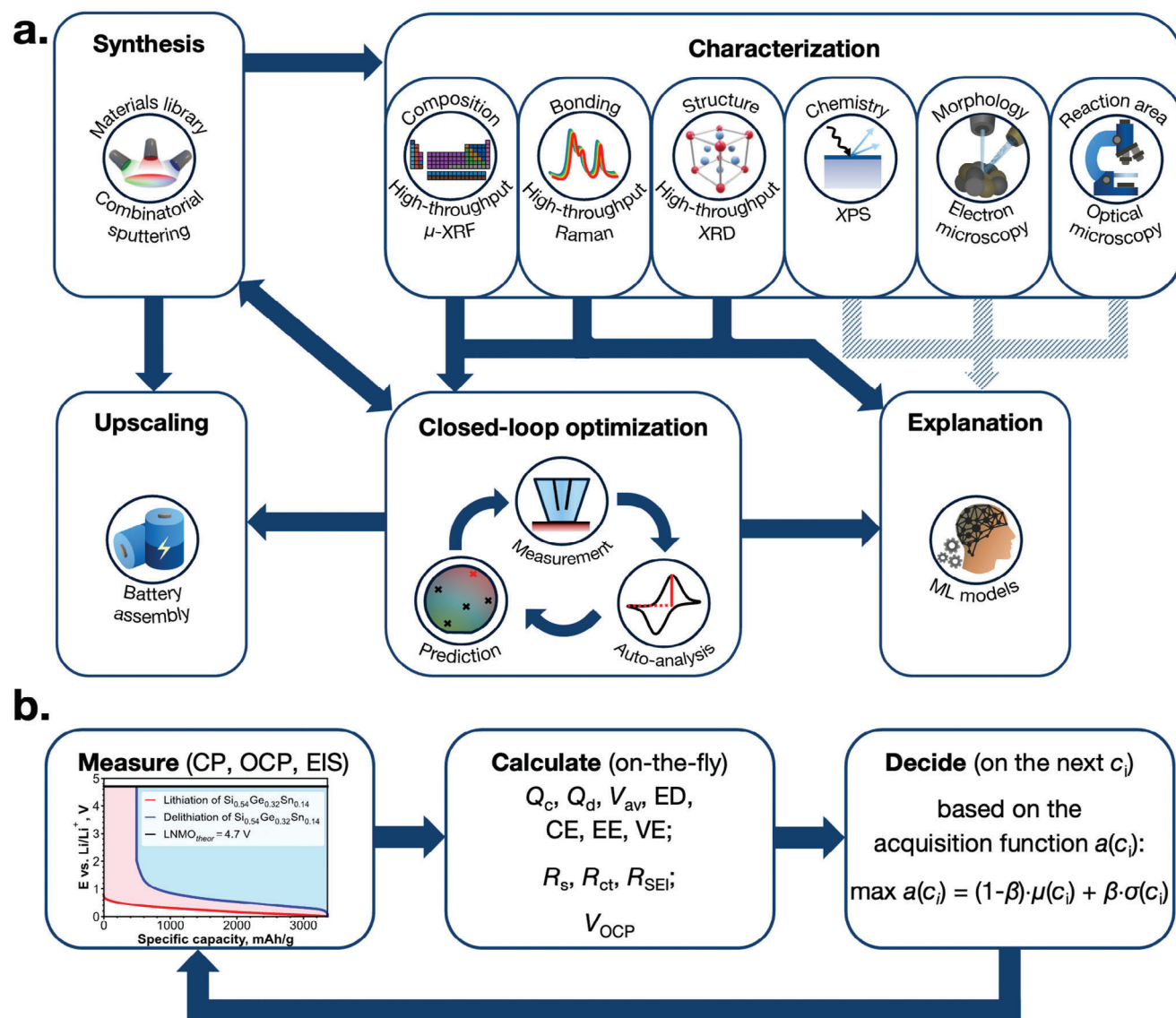
Figure 1. The present experimental workflow consists of a synthesis unit (combinatorial magnetron sputtering); units for characterization of elemental composition (high-throughput micro-X-ray fluorescence (μ-XRF)), local vibrational properties (high-throughput Raman), crystal structure (high-throughput XRD), surface chemical analysis (X-ray photoelectron spectroscopy (XPS)), morphology (scanning electron microscopy (SEM)), surface area measurements (optical microscopy); a closed-loop optimization unit (high-throughput SDC coupled with AL algorithms); upscaling unit (coin cell assembly); and an explanation unit (explainable ML models) (a), more details are available in Figure S1 (Supporting Information). Materials of interest undergo 3 dis-/charge cycles (chronopotentiometry (CP)), followed by open circuit potential (OCP) and electrochemical impedance spectroscopy (EIS) measurements. Various information is extracted (charge and discharge specific capacity at each cycle), average voltage, energy density, Coulombic, energy, and voltage efficiencies (CE, EE, VE); additionally, for EIS, the spectra are fitted, and solution, charge transfer and solid electrolyte interphase (SEI) resistances are calculated (Figure S2, Supporting Information). The next measurement point is selected based on the acquisition function (b).

2.2. Electrochemical Measurements Using SDC

2.2.1. Preliminary Tests

Before initiating the closed-loop experimentation, it was necessary to verify the reproducibility of the SDC measurements and select an appropriate charge/discharge procedure. In this study, only three cycles of CP were applied per measurement spot. This approach was chosen because significant changes in electrochemical performance are expected after the first cycle due to

the SEI formation. The differences between the second and third cycles provide insight into the degradation trends of the electrode materials. Additionally, since SDC is a sequential technique, minimizing the total measurement time was essential to enhance exploration efficiency.

We compared the performance of a non-optimized alloy cycled with a formation procedure (lithiation at C/5, delithiation at 1C) to that of cycling without formation (both lithiation and delithiation at 1C). While the reversible capacity after the third cycle was up to 10% higher when formation cycles were applied
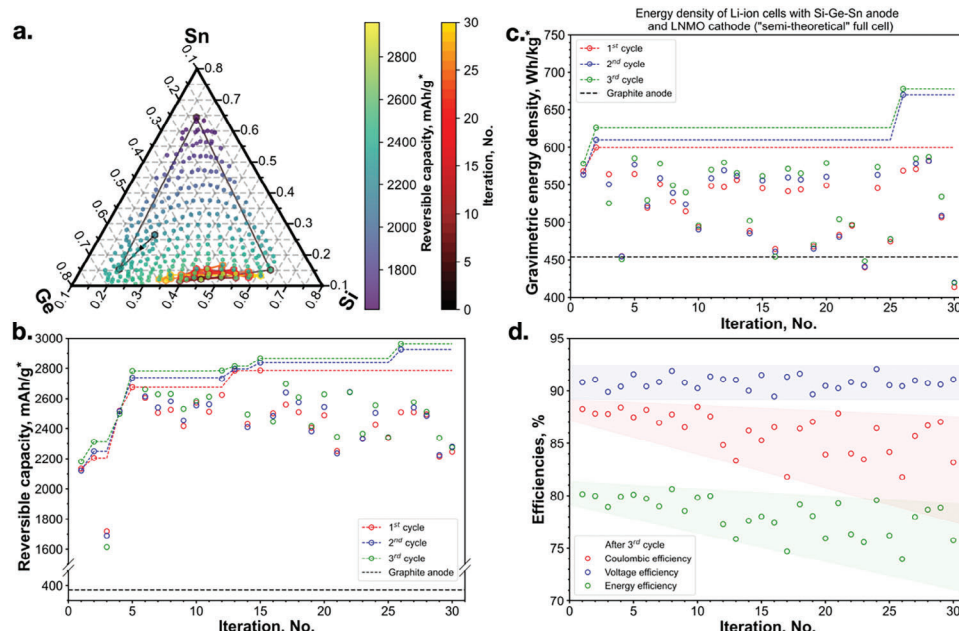
**ADVANCED
SCIENCE NEWS**

www.advancedsciencenews.com

**ADVANCED
ENERGY
MATERIALS**

www.advenergymat.de

Figure 2. Overview results from closed-loop sequential electrochemical experimentation: ternary plot of materials library, where the marker position represents the chemical composition from µ-XRF data, inner marker colors indicate the specific capacity based on experimentation and Gaussian Process (GP) regressor prediction, outer (edge) marker colors denote the SDC experiment (measurement point) number (a), measured reversible specific capacities for first (red), second (blue) and third (green) cycles, with dashed lines indicating the maximal figure of merit value over the experiment number (b); calculated gravimetric energy density using the "semi-theoretical" full cell concept assuming LNMO is used as a cathode material in comparison with graphite anode (c); Coulombic (red), voltage (blue) and energy (green) efficiencies using the "semi-theoretical" full cell concept after third cycle for all SDC experiments. The blue shaded area indicates the consistent voltage efficiencies over the iteration number, while the red and green shaded areas represent declining regions for Coulombic and energy efficiencies, respectively (d). Asterisks indicate that the specific capacities and gravimetric energy densities were calculated based on the assumption of a constant reaction area throughout the experiments (see Research limitation section).

(Figure S4a,b, Supporting Information), we opted to proceed without formation cycles in subsequent tests to increase experiment speed. We acknowledge that formation cycles can improve electrode performance, but for the purposes of rapid exploration with the SDC, the benefits were outweighed by the additional time required. Additionally, the comparative low-frequency resistances observed in EIS (Figure S4d, Supporting Information) suggest that SEI formation is similar at both C/5 and 1C rates.

Cycling at higher C rates was conducted to evaluate the high-rate performance of the alloys. The decrease in specific capacity with increasing C rate can be attributed to larger overpotentials and diffusion limitations. While capacities at 0.5 C and 1 C rates remained stable and close to the theoretical values over the cycle number, degradation effects became apparent starting from 2C, likely indicating diffusion limitation or material degradation (Figure S5a, Supporting Information). Balancing accuracy, reproducibility, and experiment time, we selected a C rate of 1 C for further tests and performed multiple measurements on the same composition to ensure results reproducibility. The uncertainty in specific capacity across all cycles remained within 2–3% (Figure S6a, Supporting Information) despite variations in reaction area across different spots (Figure S6b, Supporting Information). This suggests that the primary contribution to reversible capacity originates from the area directly under the SDC tip, allowing reliable comparisons between different spots and compositions.

2.2.2. Closed-Loop Experimentation

The closed-loop autonomous experimentation was performed to efficiently explore the Si—Ge—Sn alloy compositions with the highest specific capacity. This approach integrates autonomous electrochemical measurements using the SDC with on-the-fly data analysis and an AL algorithm to guide sequential decision-making after each measurement point on the materials library (Figure 1b). This work employs Bayesian optimization with the Gaussian Process (GP) as a surrogate model in an AL algorithm. GP was chosen for its straightforward uncertainty calculations for unexplored areas and better performance in low-to-medium dataset sizes and dimensionality spaces,[20] which aligns with the requirements of the optimization task.

During the experimental procedure, the optimizer dynamically guided the selection of upcoming measurement points from the compositional space, as illustrated in **Figure 2a**. Starting from an initial random point, the optimizer iteratively determined the next point to be measured based on real-time feedback from the electrochemical experiments after each completed iteration. In the early iterations, the optimizer explored diverse regions of the compositional space, directing measurements toward Ge-rich, Sn-rich, and Si-rich edge regions. After only three iterations, the measurement point with the highest theoretical capacity was identified, demonstrating the optimizer's ability to locate the global maximum in systems with composition-dependent

**ADVANCED
SCIENCE NEWS**

www.advancedsciencenews.com

**ADVANCED
ENERGY
MATERIALS**

www.advenergymat.de

theoretical capacities. The optimizer then gradually switched from exploration to exploitation mode, as the iteration-dependent hyperparameter of the acquisition function increasingly weighted the predicted capacity over the uncertainty, focusing on the high-capacity Si-Ge-rich region. After a total of 14 iterations, the optimizer identified the material ($Si_{0.54}Ge_{0.32}Sn_{0.14}$) with the highest measured specific capacity (Figure 2b).

The discrepancy between the samples with the highest theoretical and measured capacities could be likely attributed to high uncertainties, particularly at the edges of the materials library (Figure S3, Supporting Information), especially due to potential differences between the materials library used for the SDC and μ-XRF measurements. Unlike previous studies that used offline microscopy for area-dependent corrections, this was not possible in this autonomous experiment, as the SDC lacks an integrated microscope. Still, post-experimental microscopy showed consistency in reaction areas over all 30 measurement points (Figure S7, Supporting Information). The excessive capacities observed in the second and third cycles of the 26th experiment are likely outliers because of a significant increase in capacity after the first cycle by almost 20% (Figure 2b,c), significantly exceeding theoretical capacities. This could result from a mismatch between the XRF-measured and the actual mass loading, as the measured spot was located near the edge of the materials library.

SEM images indicated that feature sizes across the materials library were generally below 100 nm (Figure S8, Supporting Information). While smaller sizes are beneficial for minimizing kinetic limitations by enhancing Li^+ diffusion and mechanical stability, the variation in grain size was not considered a factor in this study due to limited statistical data. SEM images indicate thin films are dense, compact, and free of visible voids or discontinuities. Consistent thickness trends from XRF measurements (Figure S3c, Supporting Information) indicate minimal surface variations.

The best-performing thin-film electrodes exhibited significant improvement in specific capacities compared to a graphite anode, which was used as an internal benchmark for relative capacity trends rather than a direct performance evaluation, given the differences in electrode design (Figure 2b). A "semi-theoretical" full-cell approach[33] was used for calculating gravimetric energy densities. These calculations were derived from half-cell measurements with a Si—Ge—Sn anode and projected onto a hypothetical full-cell configuration comprising of a Si—Ge—Sn anode paired with a $LiMn_{1.5}Ni_{0.5}O_4$ (LNMO) cathode operating at a voltage of 4.7 V vs Li^+/Li. The mass of the cathode active material was adjusted to ensure capacity balance (1:1 ratio) with the anode. Calculated energy densities were 30–35% higher than those of cells with graphite anodes (Figure 2c). For the third cycle, voltage efficiencies (VE) remained consistent across all materials at ≈90–91%, while Coulombic (CE) and energy efficiencies (EE) ranged from 82–88% and 74–80%, respectively (Figure 2d). Lower efficiency values may be due to ongoing SEI formation, significant volume changes, and charge–discharge hysteresis, which are characteristic of alloy anode materials. The slight decline of CE and EE values over the iteration number (Figure 2d) could suggest a gradual deterioration of the SDC components over the extended measurement time, as the sequential electrochemical testing of 30 points on a single materials library took over 227

out of a total of 231 h (98.5% of the total experimental time, as shown in Figure S9, Supporting Information).

The differential capacity (dQ/dV) plots derived from the CP measurements by the SDC provide valuable information into the lithiation and delithiation processes for different compositions, supported by literature from Si-, Ge-, and Sn-based anodes (Figure S10, Table S1, Supporting Information). Two distinct oxidation and reduction peaks were observed across all cycles and compositions, suggesting a two-step electrochemical process.[34,35] All peaks appeared broader and less distinguishable for Sn-rich alloys, reflecting compositional influence on the electrochemical profiles.[12,36] In the first cycle, additional reduction peaks between 0.8–0.5 V could be attributed to the SEI formation,[36–38] and a minor reduction peak at ≈0.5–0.4 V is likely related to the lithiation of surface silicon oxide.[38,39]

XPS analysis (Figure S11, Table S2, Supporting Information) showed that the alloy surfaces were covered with a nonstoichiometric oxide layer, with average oxidation states of Si^{3+}, Ge^{2+}, and Sn^{4+}, but signals from elemental Si^0, Ge^0, and Sn^0 were detected as well.[40–43] Despite not being exposed to air post-deposition, the oxidation occurred, likely due to trace oxygen exposure during sputter chamber venting, inert transport to the XPS, or inside the glovebox. This oxide layer may enhance capacity retention, as glassy oxide coatings are often used to prevent material disintegration and fracture during volume changes.[44,45] However, Si oxides irreversibly form lithium silicate during lithiation,[46,47] while Ge and Sn oxides undergo a partially reversible lithiation, forming lithium oxide and lithium intermetallic compounds.[48,49] The irreversible high capacity loss in high Si-content thin films, also observed previously for a Si—Sn binary,[50] could also depend on the thickness of the oxide layer[51] and may explain the discrepancy between theoretical and measured reversible capacities.

2.3. Material Upscaling in the Coin Cell Format

Based on the closed-loop SDC discovery, the material exhibiting the best specific capacity ($Si_{0.54}Ge_{0.32}Sn_{0.14}$) was upscaled to coin cell electrode size, which corresponds to a ≈400-fold increase in area and 233-fold increase in total capacity. Upscaling was achieved by synthesizing a uniform thin film with the identified best composition on Cu foil using a combinatorial sputtering approach. Three deposition steps were required to achieve a deviation of less than 5 at. % per element from the target composition, and six depositions were needed to reduce the deviation to less than 1 at. % (Figure S12, Supporting Information). Assembled coin cells were cycled at a 1 C rate, both with and without three formation cycles at C/20. During the first formation cycle, the SEI formation started ≈1.2–0.8 V versus Li^+/Li (**Figure 3a**; Figure S11a, Supporting Information).[52] In contrast, when formation cycles were not applied, this process took place at ≈0.5–0.4 V (Figure 3b; Figure S11b, Supporting Information), likely due to the overpotential caused by the energy-intensive SEI formation process and the initial nucleation of the alloy with Li occurring without controlled conditions. Despite this difference, there was no significant impact on long-term cycling performance between cells with and without formation cycles (Figure 3c). This
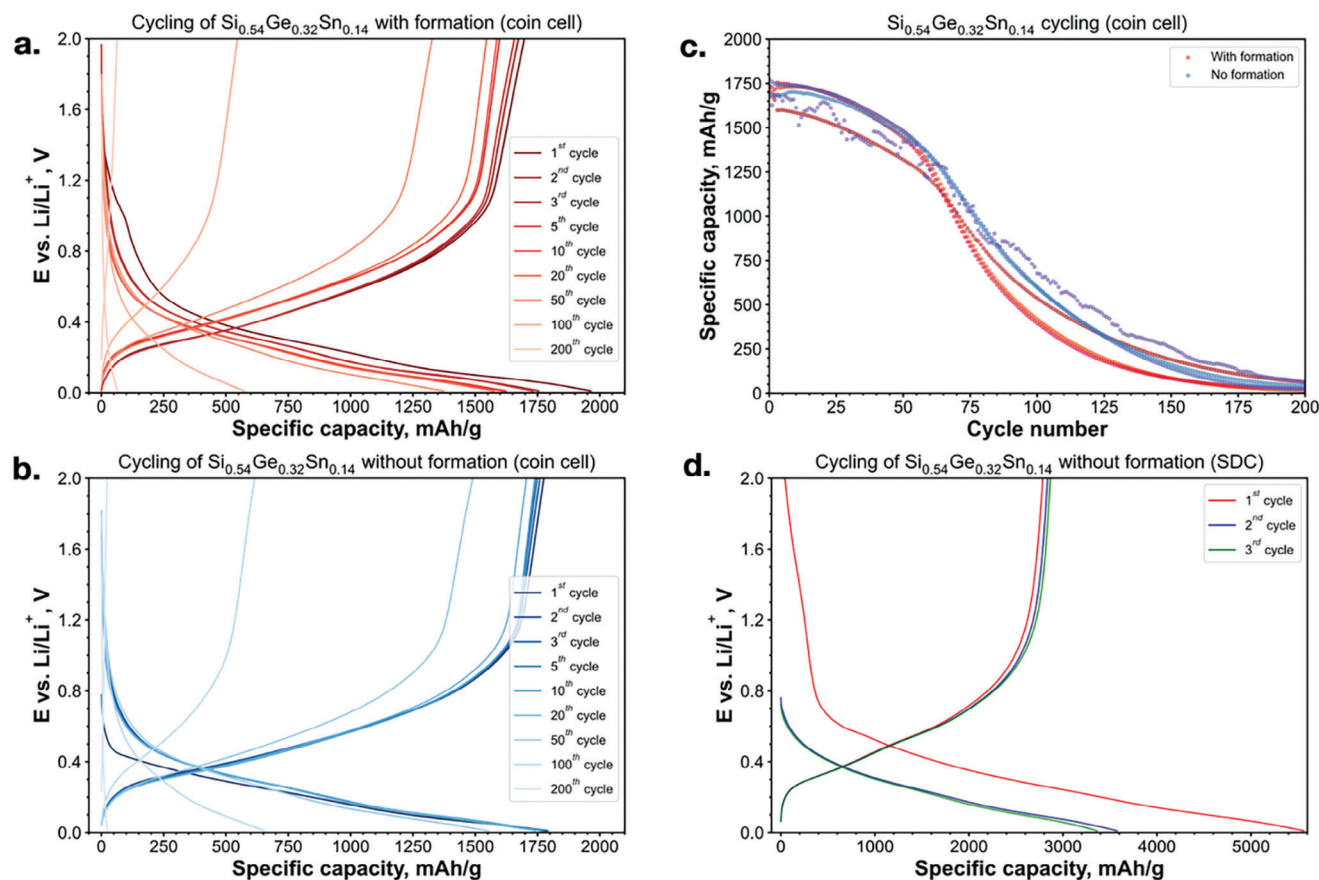
**ADVANCED
SCIENCE NEWS**

www.advancedsciencenews.com

**ADVANCED
ENERGY
MATERIALS**

www.advenergymat.de

Figure 3. Upscaling to a coin cell format and comparison with the SDC measurements for the optimized composition: dis-/charge profiles of $Si_{0.54}Ge_{0.32}Sn_{0.14}$//Li half-cell coin cells with 3 formation cycles at C/20, followed by galvanostatic cycling at 1 C rate (a), without formation, cycled at 1 C rate (b), comparison of specific capacity change over the cycle number for coin cells with and without formation cycles (c), first three cycles of $Si_{0.54}Ge_{0.32}Sn_{0.14}$ using the SDC at 1 C rate without formation (d).

suggests that even at 1 C rate, the current densities are generally still low (≈ 0.1–0.2 mA cm^{-2}), as the thickness of the anodes is ≈ 100 nm. In both cases, Coulombic efficiencies reach a maximum of $\approx 98.7\%$ after 5–7 cycles, followed by a continuous decline. Additionally, the increasing overpotential in the charge–discharge profiles over multiple cycles, particularly after the 50th cycle (Figure 3a,b), indicates accelerated electrode degradation, likely due to active material pulverization, loss of electrical contact, and continuous SEI growth, due to large volume changes during lithiation and delithiation.[53] While these potential degradation mechanisms are primarily intrinsic to the material, the thin-film configuration may further exacerbate these effects due to the absence of binders and conductive additives, potentially leading to the loss of structural integrity and electrical connectivity.

The performance of the optimized $Si_{0.54}Ge_{0.32}Sn_{0.14}$ alloy anodes was compared to that of pure Si anodes with similar thickness. Although the Si anodes initially exhibited higher specific capacities, they degraded much more rapidly than the Si—Ge—Sn anodes, consistent with previous reports comparing the cycle life of pure Si anodes versus Si—Ge and Si—Sn anodes.[54,55] The cells with the Si anode reached an 80% state-of-health after 25–29 cycles, compared to 48–59 cycles for the alloy (Figure

S14a, Supporting Information). Despite a rapid decay in semi-theoretical energy density over cycling, the energy density remained higher than the theoretical value for a semi-theoretical cell with a graphite anode. This advantage was maintained for 55–59 cycles for the alloy, compared to 20–24 cycles for the Si anode (Figure S15d, Supporting Information). These values are typical for Si-based thin-film fast-charging applications (1C and higher rates)[56] and demonstrate the advantage of the alloy material – not only due to lower volume changes but also likely to better mechanical properties, such as higher fracture resistance or higher ductility.[57] Si anodes exhibit similar electrochemical behavior with the voltage drop spike at the beginning of the first lithiation profile and similar degradation behavior with Coulombic efficiencies decrease after the fourth to fifth cycle (Figure S14b, Supporting Information). dQ/dV plots for the coin cells with a Si anode have two sharp reduction and oxidation peaks, while for $Si_{0.54}Ge_{0.32}Sn_{0.14}$, the observed peaks are broader and slightly shifted toward higher potentials. A similar behavior was observed for anodes with increased Ge and Sn content using the SDC (Figure S10b–d, Supporting Information). Nevertheless, compared to highly optimized graphite anodes, the performance of the Si—Ge—Sn anode requires further improvement, which could be enhanced by using fluorinated additives,[58] adjusting

the cycling voltage window,[59] and implementing microstructural engineering.[8]

The specific capacities of the coin cells were significantly lower than those measured using the SDC, with only up to a five-fold increase compared to graphite (Figure 3d). This discrepancy could be due to the fixed amount of active material in the coin cells, constrained by the electrode diameter, whereas in the SDC, the reaction area is less defined, and contributions from the outer SDC tip area are likely present.[16] Compared to the third cycle of the SDC experiment, the coin cells demonstrated much higher Coulombic and energy efficiencies, with similar voltage efficiencies (92–93%), suggesting that the variation arises from cell geometry rather than from the anode material itself (Figure 2d; Figure S15a–c, Supporting Information). Semi-theoretical densities were also ≈30% higher than those of cells with a graphite anode during the initial cycles, consistent with the SDC results (Figure S15d, Supporting Information). The semi-theoretical energy densities of the optimized alloy material for the third cycle were slightly higher in the coin cells (565–595 Wh kg^{-1}) compared to the SDC measurement (562 Wh g^{-1}).

2.4. High-Throughput Characterization

2.4.1. Raman Spectroscopy Results

Raman spectroscopy performed on the whole materials library (Figure S16a, Supporting Information) provided insights into the vibrational modes present in the Si—Ge—Sn thin films. Raman bands corresponding to Si–Si, Ge–Ge, and Sn–Sn vibrations and bands associated with Si—Ge, Si—Sn, and Ge—Sn bonds (Table S3, Supporting Information) were identified based on Figure S17 (Supporting Information). Compared with previously reported Raman analysis of binaries[51,52] and ternaries,[60,61] multiple unknown Sn-based bands have been observed, some of which have not been reported before, especially in the Raman shift range of 100–240 cm^{-1}. Some of these bands can be related to the E—O (E = Si, Ge, Sn) bands based on the oxide layer from XPS results (Figure S11, Supporting Information). Overlapping bands (e.g., Ge—Ge disorder-activated mode[62] at 280–285 cm^{-1} and Ge—Ge band at 290–295 cm^{-1}; Si—Sn and Si—Ge modes[61] at 387–394 cm^{-1}) and lack of reference data complicate the high-throughput analysis, making results less robust and reliable.

2.4.2. XRD Results

XRD profiles revealed broad reflections corresponding to the diamond-type cubic solid-solution phase of Si—Ge—Sn and reflections associated with the tetragonal β-Sn phase (Figure S16b, Supporting Information). No intermetallic compounds were observed in this ternary system, which aligns with expectations from the literature data.[63] The formation of a secondary β-Sn phase is expected in this ternary system due to the extremely limited solubility of Sn in Si[64] (<0.1 at.%) and Ge[65] (<0.5 at.%) at room temperature. However, the solubility of Sn in the synthesized materials library is much higher (<55 at.%, Figure S18, Supporting Information). For previously reported sputtered binaries, no crystalline phase was found for <28 at.% of Sn in Si,[66]

and <42 at.% in Ge.[67,68] This is not an unexpected result, as magnetron sputtering is a non-equilibrium synthesis technique.[69]

The qualitative interpretation of the XRD data is challenging due to its low signal-to-noise ratio, low thin-film crystallinity, and limited number of distinguishable reflections. The observed (111) reflection shifts with varying compositions, indicating solid solution behavior with a unit cell parameter variation of almost 10% (Figure S19, Supporting Information). This degree of structural change suggests that thin films are better described as nanocrystalline rather than purely amorphous. As Si atoms are smaller than Ge and especially Sn, it can be assumed that the unit cell parameter is increasing by incorporating Ge and Sn into the cubic phase, following empirical Vegard's law. The observed deviation between the theoretical and fitted unit cell parameters can be attributed to the high fit uncertainty and potential peak shifts due to microstrain present in the thin film, which could affect peak position and was not taken into account. Using Scherrer's equation, assuming no strain contribution to peak broadening, the estimated crystallite sizes are in the range of 1–4 nm for cubic Si—Ge—Sn and 5–10 nm for tetragonal β-Sn. These values correspond to the coherence length of the crystalline domains, indicating a nanocrystalline nature of the thin films.

2.5. Data-Driven Analysis

2.5.1. Principal Component Analysis (PCA)

PCA can serve as a rapid method for cluster identification and correlation detection by providing low-dimensional representations of multidimensional datasets ready for visual inspection,[70] as well as a featurization method for ML modeling. The analysis was conducted on raw background-subtracted Raman and XRD single-domain datasets.

PCA captured smooth transitions in vibrational and structural features correlated with chemical composition. PCA based solely on Raman spectra (**Figure 4a**) revealed three classes corresponding to Si-rich, Ge-rich, and Sn-rich compositions, with transition in between. The three first principal components (PCs) capture a substantial portion of the variance — 97.8% of the variance, with individual contributions of 87.9, 7.6, and 2.3% for each PC, respectively. The first PC (Figure 4c) does not exhibit any specific feature besides a peak at 280–290 cm^{-1}, corresponding to the Ge—Ge band, which helps to differentiate between Si-rich. The second PC resembles the features from Sn-rich spectra at 100–150 cm^{-1}, as well as the peak at ≈260 cm^{-1}, corresponding to the Ge—Sn band. The third PC has some Ge-rich spectra features (e.g., Ge—Ge and Si—Ge bands).

In contrast, PCA based on XRD patterns (Figure 4b) identified two main clusters: one corresponding to the cubic phase, which shows a clear trend in the unit cell parameter change with composition, and another associated with the presence of a secondary phase. This indicates a smooth property transition over the broad compositional space, characteristic of solid-state solutions, whereas some Sn-rich compositions exhibit distinct and well-defined features. However, the three first PCs accounted for merely 19.2% of the total variance (14.1, 3.6, and 1.5% for each PC). The minimal variance the leading principal components
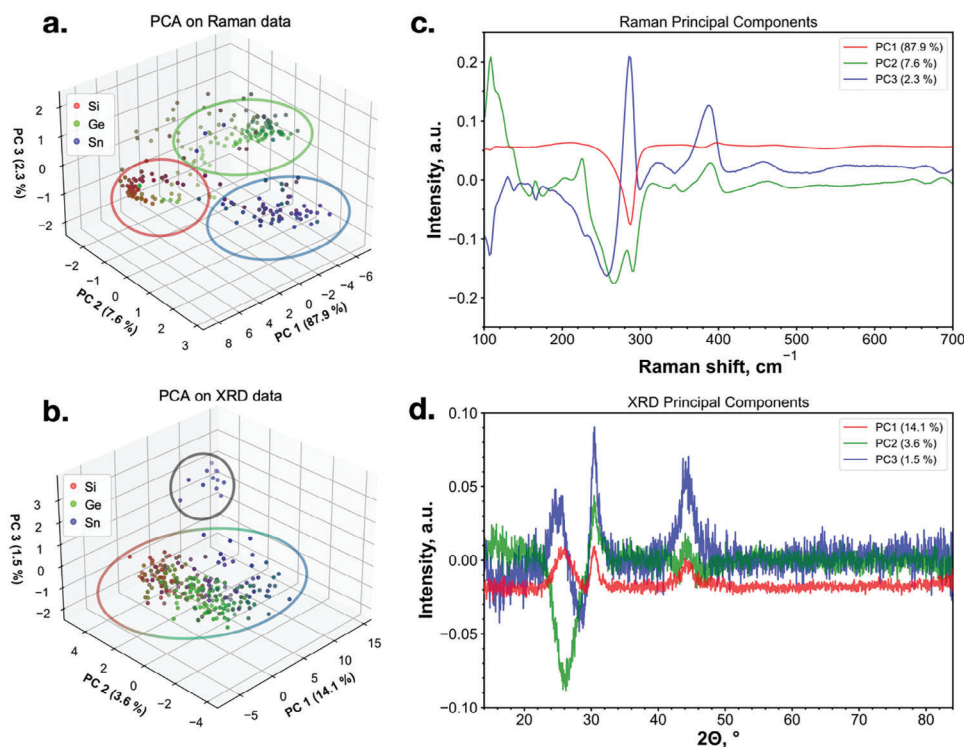
Figure 4. PCA analysis: 3D scores plot of 3 PCs from PCA based on Raman data (a): three clusters were qualitatively identified for Raman PCs, indicated by red, green, and blue ellipses. 3D scores plot of 3 PCs from PCA based on XRD data (b): two clusters were qualitatively identified for XRD data, indicated by red-green-blue and black ellipses. Percentages on the axes indicate explained variability for specific PC. The colors of the markers indicate the chemical composition of each spot from the μ-XRF: Si content corresponds to *R*-value, Ge – to *G*-value, Sn – to *B*-value of RGB color value. PCA loadings plots: the first three PC for Raman data (c), for XRD data (d).

captured could indicate a low peak-to-noise ratio within the data (Figure 4d).

2.5.2. Regression Models and Feature Importance Analysis

To explore the composition–structure–property relationships, explainable ML models were built, using chemical composition and thin-film thickness derived from mass loadings (from μ-XRF), local vibrational properties (from Raman), and crystal structure (from XRD) of the materials libraries as input features. The electrochemical performance (from SDC experiments) served as a target variable. A Random Forest (RF) regressor was employed, given its robustness to noise and invariance to feature scaling.[71] To achieve explainability, feature importance analysis and SHAP (Shapley additive explanations) were applied to the trained ML models to identify how the individual features impacted the predicted electrochemical performance and obtain insides into the underlying physicochemical properties. These ML models aim to predict specific capacity values while identifying critical features contributing to performance. By linking these features to desirable properties, the models could facilitate rapid capacity estimation using non-destructive measurement techniques, potentially reducing reliance on time-intensive electrochemical measurements.

The multidomain ML model based on Raman and XRD raw data achieved R^2 values of 0.869 ± 0.012 for the train and 0.871

for the test datasets (**Figure 5**a), indicating good predictive performance and generalization. However, the model underperforms at the extreme capacity values, likely due to the presence of outliers in the high-capacity region and limited experimental data points in the low-capacity region (Figure 5b). While excluding the compositional data from μ-XRF reduced the model's predictive power (Table S4, Supporting Information), this model was selected for detailed discussion to focus on structural and vibrational features directly related to material properties. Using a lower dimensional representation of the raw data – in the form of the fitted features or PCs could slightly improve the performance of the multidomain models: R^2 values for the test dataset are 0.882 and 0.895, respectively.

Feature importance analysis (using SHAP and traditional methods) of the ML model based on Raman and XRD raw data revealed the specific regions in Raman and XRD data significantly impacted the model's prediction. In Raman spectra, regions at 120–130 and 225–240 cm^{-1} contributed the most to the model's output (Figure 5c; Figure S20a, Supporting Information). The low Raman shift region negatively impacts the predicted capacity and could be attributed to Sn–Sn vibrations in β-Sn[72] and Sn–O vibrations in tin oxides.[73,74] The high Raman shift region contributes positively to the capacity and is more challenging to interpret due to the lack of literature data. XRD reflections related to the β-Sn phase (30.0°–32.0° and 43.0°–45.5°) showed high importance and contributed negatively to the model output (Figure 5d; Figure S20b, Supporting Information). The
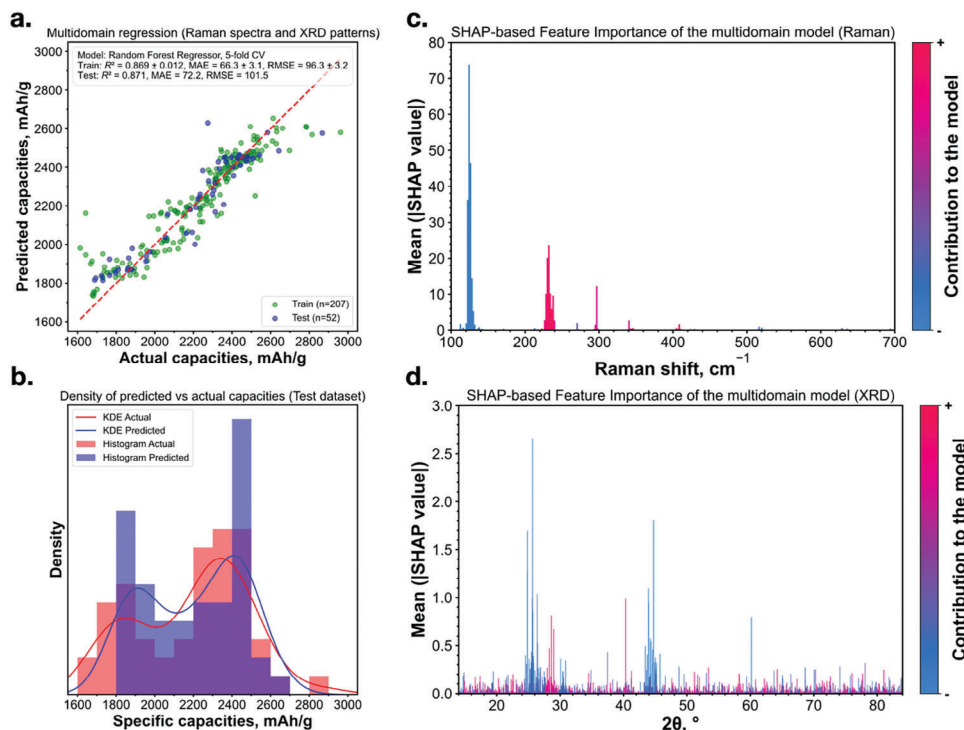
ADVANCED
SCIENCE NEWS

www.advancedsciencenews.com

ADVANCED
ENERGY
MATERIALS

www.advenergymat.de

Figure 5. Multidomain analysis based on the combined dataset consisting of Raman spectra and XRD patterns: RF regression model performance, comparing actual (from the SDC and GP regression experiment) versus predicted specific capacities (a). b) The distribution of actual versus predicted capacities for the test dataset: the density plot combines a kernel density estimate (KDE, solid line) with a histogram (bars). SHAP feature importances from the mean absolute SHAP values for the regression model, shown for (c) Raman spectra and (d) XRD patterns. SHAP values represent the impact of each feature on the model, with colors indicating the contribution sign. For instance, high SHAP values paired with a blue color suggest that a selected feature significantly decreases the specific capacity.

contribution related to the (111) broad reflection of the cubic Si—Ge—Sn phase changes sign ≈27.5°, corresponding to chemical composition variation.

The single-domain ML model built solely on raw Raman data performs comparably to the multidomain model. In contrast, the XRD-based single-domain model performed significantly worse (Table S4, Supporting Information). The performance of the feature-based models from the fitting and wavelet transformation[75] of Raman is comparable to that of those built on raw data, suggesting that the extracted features captured information similar to the raw data without offering additional insights (Figures S21–S23, Supporting Information).

Given that the theoretical capacity for the ternary system is a function of composition, we built additional models using only compositional inputs, with and without thickness data. Both models performed well, achieving R^2 values above 0.94 for both test and train datasets (Figure S24, Supporting Information). This suggests that the composition alone is sufficient to explain most of the observed variations in predicted capacities.

Based on the performances of the single- and multidomain ML models (Table S4, Supporting Information), the relationship between composition, structure, and properties appears to be sequential, with composition determining short-range local coordination, which significantly affects electrochemical performance. In contrast, long-range structural properties have minimal impact in polycrystalline materials, emphasizing the relative impor-

tance of short-range interactions and local atomic environments as the key contributors to capacity changes.

2.5.3. Correlations Interpretation

Pearson correlation heatmaps were constructed based on both raw (**Figure 6**a; Figure S25, Supporting Information) and feature-engineered data (Figure S26, Supporting Information) to identify highly correlated features and trends. Regions corresponding to XRD peaks show the strongest correlations over almost the whole Raman spectra range. Additionally, correlations for features identified via feature importance analysis of ML models were also plotted, showing how vibrational and crystallographic features co-evolve with composition (Figure 6b–g).

The increase in the lattice constant of the cubic phase is primarily driven by compositional changes (Figure 6b), which could be supported by Figure 6c, as specific capacity shows an almost linear relationship with Sn content.

Sn-rich compositions exhibit distinct features, such as Sn—Sn and Sn—O Raman bands, which serve as strong indicators of poor capacity performance. Sn—Sn Raman bands associated with the β-Sn phase are observable even for the material without the secondary phases, according to XRD (Figure 6a,d). β-Sn nanocrystallites as a secondary phase could also lead to inhomogeneous expansion and sources of localized stress in the alloy, potentially leading to their delamination from the matrix.[76]
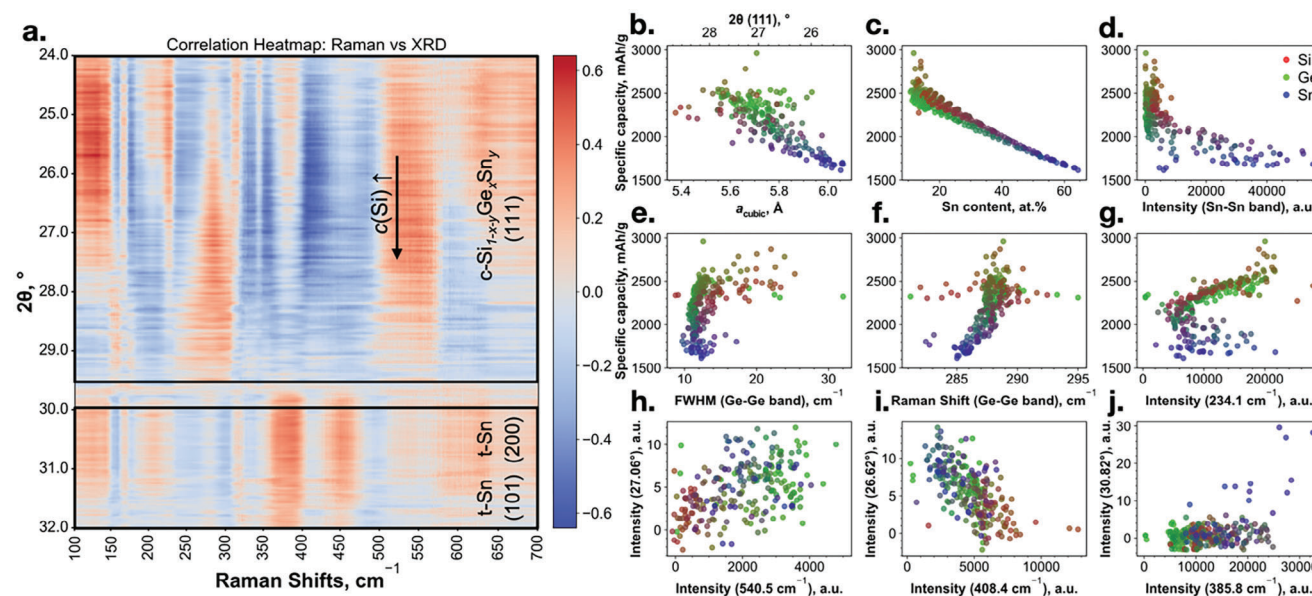
**ADVANCED
SCIENCE NEWS**

www.advancedsciencenews.com

**ADVANCED
ENERGY
MATERIALS**

www.advenergymat.de

Figure 6. Correlation matrix section from Raman spectra and XRD patterns between 2θ angles of 24° and 32°. Positive Pearson correlation coefficients between intensities at specific Raman shift values and corresponding 2θ values are shown in red, while negative correlations are in blue (a). Correlation plots for key features versus specific capacity. These features include unit cell parameter of the cubic phase and 2θ values of (111) reflections (b), Sn content (in at. %, c), the intensity of Sn—Sn Raman band ($\approx$125–135 cm^{-1}), d), FWHM (e) and Raman shift position (f) for Ge—Ge Raman band, Raman intensity at 234.1 cm^{-1} (g). Additional correlation plots from selected Raman and XRD raw data are shown in panels (h–j).

The Ge—Ge Raman band appears to be another surrogate for capacity prediction. The peak width is narrower for Ge-rich compositions but broadens for Si-rich compositions due to the disorder and compressive strain introduced by Si atoms (Figure 6e). Due to the same reasons, this Raman band shifts toward the high-frequency range for Si-rich compositions, while the opposite shift is observed for Sn-rich compositions[62] (Figure 6f). The correlation heatmap also reveals the same trends for the widths, as the high-correlation region in the Raman spectra (275–290 cm^{-1}) broadens for Si-rich compositions at higher 2θ values (27.5°–28.5°), indicating increased Si content (Figure 6a).

The intensity at 234.1 cm^{-1}, which corresponds to high feature importance and SHAP values (Figure 5c) positively correlates with Ge- and Si-rich compositions, while inverse correlations appear in the Sn-rich region (Figure 6g). This may result from two overlapping peaks, supported by Figure S17 (Supporting Information): a sharp peak associated with Sn vibrations and a broader low-frequency shoulder potentially related to Ge–Sn or Si–Ge vibrations in the oxide matrix. The broad peak may also be an artifact from background subtraction.

The XRD patterns, which at 2θ of $\approx$27.0° have high intensity and are associated with the Ge-rich materials, can help to identify additional Raman bands, such as the second-order Ge—Ge band at $\approx$540 cm^{-1} (Figure 6h), which has quite low intensity. The Raman shift range of 385–395 cm^{-1} is more indicative of the Si—Sn band than the Si—Ge band, with low intensity observed for Ge-rich compositions at 385.8 cm^{-1} (Figure 6j). On the other side, the Si—Ge band is likely shifted toward higher frequencies in this region (Figure 6i). Although the two phases suggest metallic tin segregation from the ternary alloy, the intensity of the Si—Sn band is higher for two-phase materials than for single-phase ones. The increase in Raman intensity in materials with a secondary phase requires further investigation but may stem from a higher amount of Si—Sn bonds at the phase boundaries. Notably, for 2θ values corresponding to β-Sn reflections, the correlation coefficient for the Raman shift regions related to the Sn—Sn band of β-Sn is lower than for the Si—Sn band region.

2.6. Research Limitations

The SDC offers high precision but low accuracy for minutes- and hours-long electrochemical experimentation in non-aqueous media. The low accuracy in exploratory SDC measurements is nonnegligible. To apply a consistent C rate across all materials for better comparability, the reaction volume must be calculated as the product of the measurement area and mass loading, each of which is measured by independent instrumentation with its own uncertainties. In particular, the exposed working electrode area under the SDC tip is challenging to define precisely, as potential leakage might alter the actual reaction area during measurements. While suitable for comparing materials within single or multiple materials libraries, the SDC might not be well-suited for quantitative comparisons with fully assembled coin cells, which typically offer both high precision and accuracy for extensive (e.g., mass- or area-dependent) properties (Figure S27, Supporting Information). However, different cell geometries for the same battery chemistry can show significant variations when, for instance, longevity is studied,[77] indicating that coin cells may not always be the best choice for upscaling.

Adjusting the reaction area variations after the electrochemical measurement in real-time was impossible, as no optical microscope integrated with the SDC, further affecting the AL algorithm

**ADVANCED
SCIENCE NEWS**

www.advancedsciencenews.com

**ADVANCED
ENERGY
MATERIALS**

www.advenergymat.de

decisions and experimental outcomes. The SDC is valuable for understanding electrochemical reactivity, particularly for novel and metastable materials synthesized at the thin-film scale, and for drawing preliminary conclusions on material performance. However, it is not ideal for evaluating long-term performance due to longer experimental times.

While this research utilized GP regression to predict some of the specific capacity values, a complete high-throughput screening of the entire materials library or a fully exploratory mode of Bayesian optimization would have been preferable for explanatory purposes. GP regression predictions can introduce bias, and in this study, the experimental dataset was unbalanced, with most measurements concentrated in the Si- and Ge-rich regions, while the Sn-rich region remained largely unexplored. This imbalance in the target values may have affected the performance of the RF models.

Despite maintaining near identical anode thicknesses in the current study to ensure consistency between the SDC and coin cell electrochemical performance, the scaling to thicker electrodes with realistic loadings with a few mAh cm^{-2} requires further investigation. Future studies should systematically explore the influence of film thickness on the composition–structure–property relationships, facilitating the potential commercialization of the optimized materials.

Magnetron sputtering enabled the exploration of material compositions and phases far from equilibrium, but its scalability for producing thick electrodes is limited. Future work will focus on translating these insights to scalable synthesis techniques while optimizing electrode architectures and processing conditions to bridge the gap between material discovery and practical applications.

3. Conclusion

This study demonstrates a transformative approach that integrates high-throughput experimental characterization, autonomous data-driven robotics, and ML approaches to accelerate the exploration, discovery, and understanding of advanced battery materials. Specifically, this work represents the successful implementation of the SDC for the autonomous exploration of state-of-the-art electrode materials for non-aqueous batteries. Integrating this setup with an on-the-fly analysis server and sequential learning algorithms enabled dynamic, real-time data-driven experimentation that rapidly identified high-capacity Si—Ge—Sn alloy anodes. The optimized compositions were upscaled to the coin cell format, enabling long-term cycle life evaluation. While still using thin films, this intermediate step bridged millimeter-scale discovery with validation in standardized battery formats, advancing toward practical electrode designs. Upscaled to coin cells, the optimized anodes exhibited almost a fivefold increase in specific capacity and a 30% improvement in gravimetric energy density over conventional graphite anodes. Furthermore, these alloys showed a longer cycle life than pure Si anodes, highlighting the potential for practical applications, commercialization, and impactful advancements in battery technology.

ML analysis identified key Raman and XRD features that directly and indirectly correlate with the material electrochemical performance. Correlations analysis revealed how compositional variations drive systematic changes in both local bonding environments and crystallographic structures, highlighting the interplay between short- and long-range order. XPS analysis also indicated that surface oxides could contribute to capacity discrepancies, providing further insights into the performance of these anode materials.

Integrating the ML predictions based on different modalities of material properties directly into the closed-loop experimental process could further enhance workflow efficiency, leading to improved decision-making and accelerating materials discovery.

This research contributes to advancing materials discovery and optimization, presenting a data-driven experimental framework that accelerates the discovery process while ensuring comprehensive characterization. This work addresses current challenges in sustainable energy storage and offers a blueprint for accelerated discovery and optimization across various domains in materials science.

4. Experimental Section

Materials Library Synthesis: Thin-film materials libraries of Si—Ge—Sn alloys were synthesized by magnetron co-sputtering in an Ar (5N purity, MTI IndustrieGase AG, Germany) atmosphere at room temperature (RT). The sputter chamber (Creamet 400 multi3, Creavac, Germany) with sputter-up configuration had three confocal 2″ cathodes (one operable in DC mode and two operable in RF mode) located on a horizontal circle with circular arcs of 120° between them and one 4″ cathode (RF) located in the center of this circle. The sputter chamber was integrated inside an argon glovebox (<0.1 ppm H$_2$O, <1.0 ppm O$_2$; SylaTech, Germany). Si wafers (CZ-Si wafer, 4″ diameter, 525 ± 25 μm thickness, (100)-plane, 1-side polished, p-type (B-doped), 1–10 Ohm, MicroChemicals, Germany) were used as substrates for materials libraries used for electrochemical characterization, XRD and XPS, while sapphire wafers (4″ diameter, 650 ± 25 μm thickness, C(0001)-plane, 1-side polished, Siegert Wafer, Germany) were used as substrates for materials libraries used for μ-XRF and Raman characterization. An RF bias was applied to the substrate before sputtering to clean the surface (P = 75 W, DC mode, t = 600 s, p(Ar) = 6.1 × 10^{-3} mbar). A thin film layer of Cu was sputtered (P = 200 W, t = 1800 s, DC mode, p(Ar) = 4.3 × 10^{-3} mbar) as a current collector layer from Cu target (4 N purity, 100 mm diameter, 5 mm thickness, EvoChem, Germany). For co-sputtering, Si (P = 80 W, DC mode), Ge (P = 40 W, RF mode), and Sn (P = 20 W, RF mode) were sputtered (t = 9000 s, p(Ar) = 4.0 10^{-2} mbar) from Si (5N purity, polycrystalline, p-type (B-doped), 50 mm diameter, 3 mm thickness, In-bonded to Cu, EvoChem, Germany), Ge (5N purity, polycrystalline, p-type (B-doped), 50 mm diameter, 3 mm thickness, In-bonded to Cu, EvoChem, Germany), Sn (4 N purity, 50 mm diameter, 5 mm thickness, Robeko, Germany) targets. The substrate used for the preliminary SDC tests was rotated during co-sputtering at a speed of 90° s^{-1} to obtain uniform thickness and elemental distribution. The co-sputter time was longer (t = 10 h) for the sample used in the XRD measurement to be able to collect enough signal despite likely low coherence length. Additionally, for this sample, a layer of Cu was not deposited, and a thin layer of Cr was sputtered (P = 50 W, RF mode, p(Ar) = 4.4 × 10^{-3} mbar, t = 240 s) from Cr target (3 N5 purity, 50 mm diameter, 5 mm thickness, EvoChem, Germany) to avoid alloy oxidation due to longer transportation times. The overview of all synthesized materials libraries is shown in Table S5 (Supporting Information).

Electrochemical Experimentation Using SDC: SDC setup inside an argon glovebox (<0.5 ppm H$_2$O, <0.5 ppm O$_2$; MBraun UNIlab Pro) was used to run autonomous electrochemical experimentation. The sputtered materials library was used as a working electrode (WE), Li on Pt wire as a counter electrode (CE), and Li on Cu wire as a quasi-reference electrode (RE). Li as a CE was used in excess to ensure it would not limit the electrochemical reactions at the working electrode. CE and RE were located and screwed into the Teflon SDC cell body, with a minimal distance between WE, CE, and RE. All electrochemical procedures were run using an

**ADVANCED
SCIENCE NEWS**

www.advancedsciencenews.com

**ADVANCED
ENERGY
MATERIALS**

www.advenergymat.de

Autolab PGSTAT302N potentiostat galvanostat (Metrohm Autolab, the Netherlands). A photograph of the SDC setup during an experiment is shown in Figure S28 (Supporting Information). A more detailed description of the SDC setup, the cell design, and CE and RE preparation procedures could be found elsewhere.[16] Prior to closed-loop experimentation, reproducibility tests and selection of the C rate (from C/5 to 10C) were performed on the same Si—Ge—Sn anode material. The selected sequence of electrochemical experiments included three cycles of open circuit potential (OCP) – electrochemical impedance spectroscopy (EIS) – chronopotentiometry (dis-/charge, CP) – OCP – EIS. The OCP was measured for 90 s immediately after touchdown contact with the substrate and for 300 s after the CP procedure. EIS was acquired at the OCP potential at 1 MHz to 0.1 Hz frequency range with 10 mV root mean square (RMS) amplitude. CP was performed at 1C dis-/charge rate with a cut-off potential of 0.01 and 2.00 V versus Li^+/Li. The calculation of the C rate at every measurement point was based on the atomic fractions of elements and not weight fractions, resulting in an actual applied C rate between 1.2 C–1.5 C instead of 1 C, which was deemed within the margin of error that originates from other sources of uncertainties. All extensive figures of merit (specific capacities and areal resistances) were calculated based on the SDC tip area (Figure S5b, Supporting Information). The theoretical capacities and 1 C rate currents were calculated based on composition and mass loading data from μ-XRF for each point of the materials library and for optimized materials sputtered on a Cu foil.

Closed-Loop Sequential Experimentation: The experimental sequence of experiments was orchestrated using the Hierarchical Experimental Laboratory Automation and Orchestration (HELAO) framework.[21] The sequential experiments on 30 measurement points were performed for a single materials library. The Bayesian Optimization with Gaussian Process (GP) regressor as a surrogate model from the "sklearn" package implemented in the HELAO framework was used to predict the specific capacity on a grid with 259 compositions based on the measurement results after each experimental sequence and selected the next measurement point based on the maximal value of the acquisition function. The input values for the optimizer were atomic concentrations of Si, Ge, and Sn from μ-XRF. GP used a combination of Constant, Matérn, and White Kernels, and the function minimization using the limited-memory Broyden–Fletcher—Goldfarb–Shanno with Box constraints (FMIN- L-BFGS-B) optimizer. Automatic outlier detection was implemented in order to exclude outliers from the sequential learning model if the capacity exceeded the theoretical one by more than 25% or was less than 25%. The exploration–exploitation trade-off of the acquisition function $a(c_i) = (1 - \beta) \times \mu(c_i) + \beta \times \sigma(c_i)$, where μ − mean, σ − variance from GP regression, c_i – concentrations of Si, Ge, and Sn) was driven by the iteration-dependent hyperparameter $\beta = 0.6 \times exp(-0.06 \times n) + 0.2$, where n is the number of the experiment (iteration).

The analysis action server of HELAO was programmed to be capable of on-the-fly extraction and calculation of figures of merits at the end of the electrochemical procedures on each measurement point, for example, gravimetric dis-/charge capacity, energy, voltage and Coulombic efficiencies, gravimetric energy density using "semi-theoretical" full cell concept with $LiNi_{0.5}Mn_{1.5}O_2$ (LNMO) as a counter electrode (assuming average de-/lithiation potential of 4.7 V versus Li^+/Li and specific capacity of 140 mAh g^{-1}, Q_c/Q_a = 1/1 ratio and based on the mass of anode thin film and LNMO only)[33] from CP for each cycle; averaged OCP and standard deviation after 5 min of relaxation after each cycle. Fitting of the EIS spectra was implemented as well based on the impedance.py package;[78] the selection of the equivalent circuit was performed on the fly based on the number of local maxima in Nyquist plots and χ^2-values of the fits (see Figure S2, Supporting Information). The uncertainties for all resistance elements (R), constant phase elements (CPEs), and Warburg elements (W) were calculated as well.

Upscaling: A thin film with an optimized chemical composition, as determined from the SDC experiment, was deposited onto a copper foil substrate (10 mm in diameter) using magnetron sputtering. The chemical composition of the thin films was analyzed after each deposition using micro-X-ray fluorescence (μ-XRF). Sputtering conditions, specifically the power rates of the targets, were sequentially adjusted to achieve an atomic composition error of ≤1% per element (Figure S12, Supporting Information). Prior to sputtering, the substrate surface was cleaned by applying an RF bias (P = 75 W, DC mode, t = 600 s, $p(Ar)$ = 6.1 × 10^{-3} mbar). The optimized deposition conditions involved co-sputtering of Si (P = 87 W, DC mode), Ge (P = 27 W, RF mode), and Sn (P = 14 W, RF mode) were co-sputtered ($p(Ar)$ = 4.4 × 10^{-3} mbar, t = 1800 s). The substrate was rotated at a speed of 90° s^{-1} to obtain uniform thickness and elemental distribution. For comparison, Si thin films were sputtered on Cu foil using the abovementioned procedure (P = 87 W, DC mode, $p(Ar)$ = 4.4 × 10^{-3} mbar, t = 2220 s), sputter time was adjusted to get the comparable thin-film thickness as for alloy thin films.

The cut electrodes were transferred to another glovebox using a gas-tight transport chamber for cell assembly. Prior to assembly, the stainless steel CR2032 coin cell parts (Pi-KEM, UK) were washed in an ultrasonic bath filled with isopropanol. Cleaned coin cell parts and polypropylene (PP)-polyethylene (PE)-polypropylene (PP) 3-layered separators (Celgard 2325, China) were dried in an oven at 80 °C overnight. Half-cell coin cells were assembled inside an argon-filled glovebox (<1.0 ppm H_2O, <1.0 ppm O_2; MBraun UNIlab Pro, Germany) using a copper foil with the sputtered alloy thin film (15 mm diameter), cut thick lithium ribbon metal disks to ensure an excess lithium supply and avoid capacity limitations during cycling (16 mm diameter, 0.5 mm thickness, 99.9% trace metal basis, Sigma-Aldrich, Germany), separators (18 mm diameter). Fifty microliters of 1 M $LiPF_6$ in a mixture of ethylene carbonate and ethyl methyl carbonate (EC: EMC, 30:70 wt.%) electrolyte (E-lyte, Germany) was added to each coin cell to soak the separators. After manual stacking, the coin cells were pressed together using an electric crimper machine (MSK-160E, MTI Corporation, China). The cells rested for at least 6 hours before electrochemical cycling to ensure proper wetting. For each electrochemical procedure, 3 coin cells were cycling for the proper statistical distribution.

Charge–discharge electrochemical cycling of the assembled coin cells in a temperature-controlled chamber at 20 °C was performed using a battery cycler unit (LBT21084-5, Arbin Instruments, United States). Assembled coin cells were cycled for 500 cycles between 0.01 and 2.00 V at 1 C rate for charge and discharge, with and without 3 cycles of formation at C/20 rate for charge and discharge.

Materials Library Characterization and Analysis—High-Throughput μ-XRF: The chemical compositions and areal mass loadings were analyzed using a HORIBA XGF-900 micro–X-ray Fluorescence Analytical Microscope (μ-XRF, Horiba Scientific, Japan). As it was impossible to distinguish Si from thin film and substrate, the materials libraries for the analysis were sputtered on sapphire wafers. The XRF spectra were acquired on defined grid positions for 300 s using 50 kV X-Ray energy (Rh source), 100 μm polycapillary optics, without an energy filter. The multilayer FPM function was used to determine the parameters. Calculations were performed based on the intensity of the K_α-lines of Si and Ge and the L_α-lines of Sn as a first layer, K_α-lines of Cu as a second layer, and K_α-lines of Al as a bulk layer.

Materials Library Characterization and Analysis—High-Throughput Raman: Raman spectra were recorded using a confocal Raman microscope (InVia QONTOR, Renishaw, United Kingdom) equipped with a Renishaw Centers 1AY680 detector. A green laser with a wavelength of 532 nm and nominal power of 50 mW was employed, using a 50× objective lens (Leica, Germany) in back-scatter configuration. To minimize thin-film damage, the laser power was set to 5%. Spectra were recorded on defined grid positions with batch measurement mode with the UseLiveTrack option for focus tracking before each measurement. The spectral range was from 100 to 700 cm^{-1}, and ten accumulations were made to increase the signal-to-noise ratio. The WiRE 5.5 in-built software automatically removed the cosmic rays from the spectra.

Materials Library Characterization and Analysis—High-Throughput XRD: XRD patterns were recorded using a Bruker D8 Discover X-Ray Diffractometer equipped with a Vantec-500 2D detector (Bruker AXS, Germany) in Bragg–Brentano geometry. A microfocus X-ray source (Incoatec Iμs High Brilliance) with Cu K_α X-ray radiation (λ = 0.15418 nm) was employed, operating at 50 kV and 1 mA, generating 50 W of tube power. At each measurement area of the grid, three 2D-images (frames) were taken at the $\theta/2\theta$ positions 10°/25°, 20°/45°, and 30°/65°, with a fixed angular

**ADVANCED
SCIENCE NEWS**

www.advancedsciencenews.com

**ADVANCED
ENERGY
MATERIALS**

www.advenergymat.de

increment of $10°/2\theta$. A $2.5°$ offset on θ was applied to avoid single-crystal Si-substrate peaks. 1D diffraction patterns with an angular 2θ range from $\approx 13.2°$ to $84.2°$ were integrated from these frames using Bruker DiffracEVA software.

Materials Library Characterization and Analysis—X-Ray Photoelectron Spectroscopy (XPS): X-ray Photoelectron spectroscopy (XPS) measurements were performed for 4 selected points on a materials library using a near ambient pressure (NAP)-XPS (Specs EnviroESCA, Germany), connected to the nitrogen-filled glovebox via the transfer chamber (GS Glovebox Systemtechnik GmbH, Germany). Spectra were taken with a commercial UHV system (SPECS) with a base pressure of 2×10^{-10} mbar using a monochromatized X-ray source (SPECS XR50 M, Al K$_{\alpha}$ and Ag K$_{\alpha}$, FOCUS 500 X-ray monochromator) and a hemispherical analyzer (SPECS, DLSEGD- Phoibos-Has3500). Fine spectra were acquired 10 times to capture the C1s, O1s, Si2p, Ge3p, and Sn3d$_{5/2}$ lines. CasaXPS software (version 2.3.23, Japan)[79] was used to fit the data for all XPS spectra.

Materials Library Characterization and Analysis—Scanning Electron Microscopy (SEM): The morphologies of deposited thin films were investigated using a scanning electron microscope (SEM) Apreo 2S HiVac (ThermoScientific, Germany). The materials library was fixed on a 4″ EM-Tec W4 wafer holder (Micro to Nano BV, Netherlands). An accelerating voltage of 2.0 kV, a specimen current in the range of 50–400 pA, a working distance of 10.0 mm, magnification of 25 000×, a chamber pressure of $<2 \times 10^{-6}$ mbar, an Everhart–Thornley detector in secondary electrons (SE) mode and the OptiPlan use case were used to acquire SEM images.

Materials Library Characterization and Analysis—Optical Microscopy: Prior to imaging, the reaction areas were locally washed 3 times using the SDC with EC: EMC electrolyte with a ratio of 30:70 wt.% (Elyte, Germany) for 5 min followed by drying inside the argon glovebox to remove the dried LiPF$_6$ salt excess. Optical images of the reaction area of the measurement points on materials libraries were captured using the Keyence VHX 7000 optical microscope (Keyence, Germany) at 500× magnification with the Stitching 3D Imaging option in HDR mode. To assess the reaction area of the working electrode the "maximum area" measurement function supplied by Keyence VHX software was used. Additionally, the optical images from the μ-XRF microscope were also recorded for some materials libraries.

Data Analysis and ML Methods—Feature Extraction from Raman Spectra: Raman spectra were preprocessed using PRISMA software.[80] The background removal procedure was performed by applying the asymmetric least squares baseline correction ($\log(p) = -3.0$, $\log(\lambda) = 3.0$). Spectra were fitted using Gaussian peak lineshapes, assuming the presence of 19 peaks based on the literature data and appearance of the spectra (Table S3, Supporting Information). A total of 76 features were calculated, including peak positions, FWHM, intensities at half maximum, and peak areas for each Gaussian. For wavelet decomposition, the "pywt" Python package was used, and decomposition was performed across 6 levels, which resulted in 82 features.

Data Analysis and ML Methods—Feature Extraction from XRD Patterns: Fitting and data analysis of the XRD patterns were performed using the "curve_fit" function from the "scipy-optimize" Python package, with a maximum of 20 000 iterations until convergence. Peaks were fitted using a pseudo-Voigt function under physical constraints, assuming a constant full width at half maximum (FWHM) for all peaks of the same phase. The fitting process initially assumed the presence of a diamond—ype cubic solid solution of Si—Ge—Sn and a tetragonal Sn phase based on preliminary analysis and diffraction patterns from the Materials Project dataset (mp-149 and mp-84).[81] If the fitted values fell outside the selected range or if the uncertainties exceeded acceptable limits (>2.5% for the cubic phase and >1.0% for the tetragonal phase), one or both phases were excluded from further analysis. The fitting process was repeated in cases where phases were removed. As a result, 12 features were extracted: unit cell parameters, FWHM, and peak intensities for each phase for each phase, as phase presence were extracted.

Data Analysis and ML Methods—Principal Component Analysis (PCA): PCA of 3 first components was performed using "decomposition. PCA" module of the "sklearn" Python package based on the raw Raman spectra and XRD patterns for dimensionality reduction of the features for ML, cluster identification, and initial exploration of trends and correlations. Raw data with a corrected background was centered by subtracting the mean and normalized on a per-sample basis using a min-max normalization.

Data Analysis and ML Methods—Random Forest (RF) Regression: Single- and multidomain ML models based on a Random Forest (RF) regressor were built using a "sklearn" library. As target values, reversible specific capacities from the SDC experiment after the third cycle (Q_3, mAh g^{-1}) were taken (both experimental and GP-predicted) for the whole materials library. These models incorporated various input data, including Raman spectra (raw, fitted, and PCA features, wavelet decomposition), XRD profiles (raw, fitted, and PCA features), thin-film thicknesses, and chemical composition (Si, Ge, and Sn atomic concentrations from μ-XRF). Missing XRD features were imputed, and model hyperparameters (depth of the trees, max number of features, min samples leaf and split, number of tree estimators) were optimized for each data subset via grid search. The model's tree depth is set below 20 to prevent overfitting. An 80/20 train-test split and fivefold cross-validation were used. The coefficient of determination (R^2), mean absolute error (MAE), and root mean squared error (RMSE) were selected as performance metrics for estimating model performances.

Data Analysis and ML Methods—Feature Importance and SHAP Analysis: Feature importance scores were extracted from the "feature_importances" attribute of the selected RF regression models, implemented using the "sklearn" library in Python. SHAP values, representing the contribution of each feature to the prediction, were computed using the SHAP package.[82] SHAP coefficients were derived from the "TreeExplainer" method applied to the selected RF regression models. SHAP-based feature importance analysis was done by calculating the mean of absolute SHAP values for all features, and a sign of the contribution was calculated from the sign and the value of the Pearson correlation coefficients between SHAP values and feature values.

Data Analysis and ML Methods—Correlation Analysis: A correlation analysis examined the relationships between the raw and fitted Raman and XRD data. A correlation matrix was computed to determine pairwise Pearson correlation coefficients between all features using the "df.corr" function of Python's "pandas" package. The matrix was visualized as a heatmap using the "seaborn" package. Areas with the highest absolute coefficients, representing the strongest correlations, were further analyzed to explore feature dependencies.

Supporting Information

Supporting Information is available from the Wiley Online Library or from the author.

Acknowledgements

Conflict of Interest

The authors declare no conflict of interest.

**ADVANCED
SCIENCE NEWS**

www.advancedsciencenews.com

**ADVANCED
ENERGY
MATERIALS**

www.advenergymat.de

Data Availability Statement

All data and analyses in this paper are available at https://zenodo.org/records/14002198, https://doi.org/10.5281/zenodo.10724793.

[1] M. Linder, T. Nauclér, S. Nekovar, A. Pfeiffer, N. Vekić, McKinsey Co. **2023**, https://www.mckinsey.com/industries/automotive-and-assembly/our-insights/the-race-to-decarbonize-electric-vehicle-batteries (accessed: December 2024).

[2] J. Fleischmann, D. Herring, F. Liebach, M. Linder, *McKinsey Co.* **2021**, *3*, 2003.

[3] A. R. Dehghani-Sanij, E. Tharumalingam, M. B. Dusseault, R. Fraser, *Renewable Sustainable Energy Rev.* **2019**, *104*, 192.

[4] C. Wang, C. Yang, Z. Zheng, *Adv. Sci.* **2022**, *9*, 2105213.

[5] M. N. Obrovac, L. Christensen, *Electrochem. Solid-State Lett.* **2004**, *7*, A93.

[6] C. Zhu, K. Han, D. Geng, H. Ye, X. Meng, *Electrochim. Acta* **2017**, *251*, 710.

[7] Z. Feng, W. Peng, Z. Wang, H. Guo, X. Li, G. Yan, J. Wang, *Int. J. Miner. Metall. Mater.* **2021**, *28*, 1549.

[8] P. Zheng, J. Sun, H. Liu, R. Wang, C. Liu, Y. Zhao, J. Li, Y. Zheng, X. Rui, *Batteries Supercaps* **2023**, *6*, 202200481.

[9] D. Liu, Z. Liu, X. Li, W. Xie, Q. Wang, Q. Liu, Y. Fu, D. He, *Small* **2017**, *13*, 1702000.

[10] J. Graetz, C. C. Ahn, R. Yazami, B. Fultz, *J. Electrochem. Soc.* **2004**, *151*, A698.

[11] R. A. Huggins, *J. Power Sources* **1999**, *81–82*, 13.

[12] K. Yao, N. Li, N. Li, E. Sivonxay, Y. Du, K. A. Persson, D. Su, W. Tong, *Chem. Mater.* **2023**, *35*, 2281.

[13] X. Liu, X.-Y. Wu, B. Chang, K.-X. Wang, *Energy Storage Mater.* **2020**, *30*, 146.

[14] A. W. Hassel, M. M. Lohrengel, *Electrochim. Acta* **1997**, *42*, 3327.

[15] S. Daboss, F. Rahmanian, H. S. Stein, C. Kranz, *Electrochem. Sci. Adv.* **2021**, *2*, 2100122.

[16] A. Sanin, H. S. Stein, *Chem. Mater.* **2024**, *36*, 3536.

[17] D. Muñoz-Torrero, C. Santana Santos, E. García-Quismondo, S. Dieckhöfer, T. Erichsen, J. Palma, W. Schuhmann, E. Ventosa, *RSC Adv.* **2023**, *13*, 15521.

[18] S. Dieckhöfer, W. Schuhmann, E. Ventosa, *ChemElectroChem* **2021**, *8*, 3143.

[19] B. Zhang, L. Merker, A. Sanin, H. S. Stein, *Digital Discovery* **2022**, *1*, 755.

[20] B. Rohr, H. S. Stein, D. Guevarra, Y. Wang, J. A. Haber, M. Aykol, S. K. Suram, J. M. Gregoire, *Chem. Sci.* **2020**, *11*, 2696.

[21] F. Rahmanian, J. Flowers, D. Guevarra, M. Richter, M. Fichtner, P. Donnely, J. M. Gregoire, H. S. Stein, *Adv. Mater. Interfaces* **2022**, *9*, 2101987.

[22] S. V. Kalinin, M. Ziatdinov, M. Ahmadi, A. Ghosh, K. Roccapriore, Y. Liu, R. K. Vasudevan, *Appl. Phys. Rev.* **2024**, *11*, 011314.

[23] A. Aspuru-Guzik, K. Persson, *Can. Inst. Adv. Res.* **2018**, https://mission-innovation.net/wp-content/uploads/2018/01/Mission-Innovation-IC6-Report-Materials-Acceleration-Platform-Jan-2018.pdf.

[24] H. S. Stein, J. M. Gregoire, *Chem. Sci.* **2019**, *10*, 9640.

[25] A. Benayad, D. Diddens, A. Heuer, A. N. Krishnamoorthy, M. Maiti, F. L. Cras, M. Legallais, F. Rahmanian, Y. Shin, H. Stein, M. Winter, C. Wölke, P. Yan, I. Cekic-Laskovic, *Adv. Energy Mater.* **2022**, *12*, 2102678.

[26] M. Vogler, J. Busk, H. Hajiyani, P. B. Jørgensen, N. Safaei, I. E. Castelli, F. F. Ramirez, J. Carlsson, G. Pizzi, S. Clark, F. Hanke, A. Bhowmik, H. S. Stein, *Matter* **2023**, *6*, 2647.

[27] M. Vogler, S. K. Steensen, F. F. Ramírez, L. Merker, J. Busk, J. M. Carlsson, L. H. Rieger, B. Zhang, F. Liot, G. Pizzi, F. Hanke, E. Flores, H. Hajiyani, S. Fuchs, A. Sanin, M. Gaberšček, I. E. Castelli, S. Clark, T. Vegge, A. Bhowmik, H. S. Stein, *Adv. Energy Mater.* **2024**, *14*, 2403263.

[28] N. S. Eyke, B. A. Koscher, K. F. Jensen, *Trends Chem.* **2021**, *3*, 120.

[29] F. Häse, L. M. Roch, A. Aspuru-Guzik, *Trends Chem.* **2019**, *1*, 282.

[30] "Sputtering Yield Rates", can be found under, https://www.semicore.com/reference/sputtering-yields-reference, n.d. (accessed: December 2024).

[31] J. Li, A. K. Dozier, Y. Li, F. Yang, Y.-T. Cheng, *J. Electrochem. Soc.* **2011**, *158*, A689.

[32] Q. Wu, B. Shi, J. Bareño, Y. Liu, V. A. Maroni, D. Zhai, D. W. Dees, W. Lu, *ACS Appl. Mater. Interfaces* **2018**, *10*, 3487.

[33] J. Asenbauer, A. Varzi, S. Passerini, D. Bresser, *J. Power Sources* **2020**, *473*, 228583.

[34] M. N. Obrovac, L. J. Krause, *J. Electrochem. Soc.* **2007**, *154*, A103.

[35] K. Ogata, E. Salager, C. J. Kerr, A. E. Fraser, C. Ducati, A. J. Morris, S. Hofmann, C. P. Grey, *Nat. Commun.* **2014**, *5*, 3217.

[36] M. Salah, C. Hall, P. L. Yap, M. Fabretto, *Thin Solid Films* **2024**, *796*, 140332.

[37] J. Graetz, C. C. Ahn, R. Yazami, B. Fultz, *Electrochem. Solid-State Lett.* **2003**, *6*, A194.

[38] C. Cao, H.-G. Steinrück, B. Shyam, K. H. Stone, M. F. Toney, *Nano Lett.* **2016**, *16*, 7394.

[39] K. W. Schroder, A. G. Dylla, S. J. Harris, L. J. Webb, K. J. Stevenson, *ACS Appl. Mater. Interfaces* **2014**, *6*, 21510.

[40] R. Alfonsetti, L. Lozzi, M. Passacantando, P. Picozzi, S. Santucci, *Appl. Surf. Sci.* **1993**, *70–71*, 222.

[41] O. A. Chuvenkova, E. P. Domashevskaya, S. V. Ryabtsev, D. V. Vysotskii, A. E. Popov, Y. A. Yurakov, O. Y. Vilkov, R. Ovsyannikov, N. Appathurai, S. Y. Turishchev, *J. Surf. Invest.: X-Ray Synchrotron Neutron Tech.* **2014**, *8*, 111.

[42] O. A. Chuvenkova, E. P. Domashevskaya, S. V. Ryabtsev, Y. A. Yurakov, A. E. Popov, D. A. Koyuda, D. N. Nesterov, D. E. Spirin, R. Y. Ovsyannikov, S. Y. Turishchev, *Phys. Solid State* **2015**, *57*, 153.

[43] K. Prabhakaran, T. Ogino, *Surf. Sci.* **1995**, *325*, 263.

[44] H. S. Sitinamaluwa, H. Li, K. C. Wasalathilake, A. Wolff, T. Tesfamichael, S. Zhang, C. Yan, *Nano Mater. Sci.* **2019**, *1*, 70.

[45] S. Guo, H. Li, Y. Li, Y. Han, K. Chen, G. Xu, Y. Zhu, X. Hu, *Adv. Energy Mater.* **2018**, *8*, 1800434.

[46] H. Takezawa, K. Iwamoto, S. Ito, H. Yoshizawa, *J. Power Sources* **2013**, *244*, 149.

[47] Q. Sun, B. Zhang, Z.-W. Fu, *Appl. Surf. Sci.* **2008**, *254*, 3774.

[48] J. Liu, K. Song, C. Zhu, C.-C. Chen, P. A. Van Aken, J. Maier, Y. Yu, *ACS Nano* **2014**, *8*, 7051.

[49] W. Liu, X. Huang, Z. Wang, H. Li, L. Chen, *J. Electrochem. Soc.* **1998**, *145*, 59.

[50] T. D. Hatchard, J. R. Dahn, *J. Electrochem. Soc.* **2004**, *151*, A1628.

[51] M. Schnabel, S. P. Harvey, E. Arca, C. Stetson, G. Teeter, C. Ban, P. Stradins, *ACS Appl. Mater. Interfaces* **2020**, *12*, 27017.

[52] R. Fong, U. Von Sacken, J. R. Dahn, *J. Electrochem. Soc.* **1990**, *137*, 2009.

[53] Z. Chen, A. Soltani, Y. Chen, Q. Zhang, A. Davoodi, S. Hosseinpour, W. Peukert, W. Liu, *Adv. Energy Mater.* **2022**, *12*, 2200924.

[54] M. Suzuki, J. Suzuki, K. Sekine, T. Takamura, *J. Power Sources* **2005**, *146*, 452.

[55] P. R. Abel, A. M. Chockla, Y.-M. Lin, V. C. Holmberg, J. T. Harris, B. A. Korgel, A. Heller, C. B. Mullins, *ACS Nano* **2013**, *7*, 2249.

[56] A. Mukanova, A. Jetybayeva, S.-T. Myung, S.-S. Kim, Z. Bakenov, *Mater. Today Energy* **2018**, *9*, 49.

[57] Q. Fan, B. Hao, L. Jiang, X. Yu, W. Zhang, Y. Song, S. Yun, *Results Phys.* **2021**, *25*, 104254.

[58] V. Etacheri, O. Haik, Y. Go, D. Aurbach, *Langmuir* **2012**, *28*, 965.

[59] S.-J. Lee, J.-K. Lee, S.-H. Chung, H.-Y. Lee, S.-M. Lee, H.-K. Baik, *J. Power Sources* **2001**, *97*, 191.

[60] J.-H. Fournier-Lupien, S. Mukherjee, S. Wirths, E. Pippel, N. Hayazawa, G. Mussler, J. M. Hartmann, P. Desjardins, D. Buca, O. Moutanabbir, *Appl. Phys. Lett.* **2013**, *103*, 263103.

[61] J. Schlipf, H. Tetzner, D. Spirito, C. L. Manganelli, G. Capellini, M. R. S. Huang, C. T. Koch, C. J. Clausen, A. Elsayed, M. Oehme, S. Chiussi, J. Schulze, I. A. Fischer, *J. Raman Spectrosc.* **2021**, *52*, 1167.

[62] V. R. D'Costa, J. Tolle, R. Roucka, C. D. Poweleit, J. Kouvetakis, J. Menéndez, *Solid State Commun.* **2007**, *144*, 240.

[63] G. B. Stringfellow, P. E. Greene, *J. Electrochem. Soc.* **1970**, *117*, 1075.

[64] R. W. Olesinski, G. J. Abbaschian, *Bull. Alloy Phase Diagrams* **1984**, *5*, 273.

[65] R. W. Olesinski, G. J. Abbaschian, *Bull. Alloy Phase Diagrams* **1984**, *5*, 265.

[66] T. Maruyama, H. Akagi, *J. Electrochem. Soc.* **1997**, *144*, 4350.

[67] H. Fukumoto, H. Myoren, T. Nakashita, T. Imura, Y. Osaka, *Jpn. J. Appl. Phys.* **1986**, *25*, 1312.

[68] T. Maruyama, H. Akagi, *J. Electrochem. Soc.* **1998**, *145*, 1303.

[69] H. Stein, D. Naujoks, D. Grochla, C. Khare, R. Gutkowski, S. Grützke, W. Schuhmann, A. Ludwig, *Phys. Status Solidi A* **2015**, *212*, 2798.

[70] C. Suh, A. Rajagopalan, X. Li, K. Rajan, *Data Sci. J.* **2002**, *1*, 19.

[71] A. Criminisi, J. Shotton, E. Konukoglu, *Found. Trends Comput. Graph. Vis.* **2012**, *7*, 81.

[72] S. Liu, A. C. Covian, J. A. Gardener, A. Akey, B. D. A. Levin, X. Wang, J. Liu, *Commun. Mater.* **2022**, *3*, 17.

[73] M. G. Masteghin, R. A. Silva, D. C. Cox, D. R. M. Godoi, S. R. P. Silva, M. O. Orlandi, *Phys. Chem. Chem. Phys.* **2021**, *23*, 9733.

[74] B. Eifert, M. Becker, C. T. Reindl, M. Giar, L. Zheng, A. Polity, Y. He, C. Heiliger, P. J. Klar, *Phys. Rev. Mater.* **2017**, *1*, 014602.

[75] C. Camerlingo, F. Zenone, G. M. Gaeta, R. Riccio, M. Lepore, *Meas. Sci. Technol.* **2006**, *17*, 298.

[76] J. R. Dahn, R. E. Mar, M. D. Fleischauer, M. N. Obrovac, *J. Electrochem. Soc.* **2006**, *156*, A1211.

[77] A. Smith, P. Stüble, L. Leuthner, A. Hofmann, F. Jeschull, L. Mereacre, *Batteries Supercaps* **2023**, *6*, 202300080.

[78] M. Murbach, B. Gerwe, N. Dawson-Elli, L. Tsui, *J. Open Source Software* **2020**, *5*, 2349.

[79] N. Fairley, V. Fernandez, M. Richard-Plouet, C. Guillot-Deudon, J. Walton, E. Smith, D. Flahaut, M. Greiner, M. Biesinger, S. Tougaard, D. Morgan, J. Baltrusaitis, *Appl. Surf. Sci. Adv.* **2021**, *5*, 100112.

[80] E. Flores, N. Mozhzhukhina, X. Li, P. Norby, A. Matic, T. Vegge, *Chem.: Methods* **2022**, *2*, 202100094.

[81] A. Jain, S. P. Ong, G. Hautier, W. Chen, W. D. Richards, S. Dacek, S. Cholia, D. Gunter, D. Skinner, G. Ceder, K. A. Persson, *APL Mater.* **2013**, *1*, 011002.

[82] S. M. Lundberg, S.-I. Lee, in *Adv. Neural Inf. Process. Syst.*, Vol. 30, (Eds.: I. Guyon, U. V. Luxburg, S. Bengio, H. Wallach, R. Fergus, S. Vishwanathan, R. Garnett), Curran Associates, Inc., Red Hook, NY **2017**, p. 4765.